Nozzle Geometry-Induced Vortices in Supersonic Wind Tunnels*

Kshitij Sabnis† and Holger Babinsky‡
Department of Engineering, University of Cambridge, Cambridge, CB2 1PZ, UK

Daniel S. Galbraith§ and John A. Benek¶
Air Force Research Laboratory, Wright-Patterson AFB, Ohio, United States

Streamwise-coherent structures were observed in schlieren images of a Mach 2.5 flow in an empty supersonic wind tunnel with rectangular cross-section. These features are studied using RANS computations in combination with wind tunnel experiments. The structures are identified as regions of streamwise vorticity embedded in the sidewall boundary layers. These vortices locally perturb the sidewall boundary layers, and can increase their thickness by as much as 37%. The vortices are caused by a region of separation upstream of the nozzle where there is a sharp geometry change, typical in supersonic wind tunnels with interchangeable nozzle blocks. Despite originating in the corners, the vortices are transported by secondary flows in the sidewall boundary layers so they end up near the tunnel centre-height, well away from any corners. The successful elimination of these sidewall vortices from the flow is achieved by replacing the sharp corner with a more rounded geometry, so that the flow here remains attached.

Nomenclature

H_i = incompressible boundary-layer shape factor $\left(\delta_i^*/\theta_i\right)$

M_∞ = freestream Mach number

p = static pressure

p_0 = stagnation pressure

u = streamwise velocity

u_e = streamwise velocity at the boundary-layer edge

x = streamwise coordinate, relative to the nozzle exit plane

y = vertical coordinate, relative to the floor

*Presented as Paper 2019-3073 at the AIAA Aviation 2019 Forum, Dallas, TX, 17–21 June 2019.
†PhD Student, Department of Engineering, University of Cambridge.
‡Professor in Aerodynamics, Department of Engineering, University of Cambridge, AIAA Associate Fellow.
§Engineer, Computational Sciences Centre, AFRL Aerospace Systems Directorate.
¶Director, Computational Sciences Centre, AFRL Aerospace Systems Directorate, AIAA Fellow.

z = spanwise coordinate, relative to the tunnel centreline

$\tilde{z}$ = spanwise coordinate, relative to the tunnel sidewall

δ = boundary-layer thickness (from fit to Sun & Childs (1973) model)

δ_i^* = incompressible boundary-layer displacement thickness $\left(\int_0^\delta (1 - u/u_e)\ \mathrm{d}y\right)$

θ_i = incompressible boundary-layer momentum thickness $\left(\int_0^\delta (u/u_e)\,(1 - u/u_e)\ \mathrm{d}y\right)$

ρ = density

ω_{RR} = rigid-body component of streamwise vorticity

I. Introduction

Experiments on supersonic flows are typically conducted in wind tunnels with rectangular cross-sections, which use two-dimensional nozzles. A close inspection of some schlieren images from such facilities reveals subtle streamwise-coherent features in the working sections [1–3]. These structures are only captured in the most sensitive schlieren setups, and so are generally assumed to be weak. Despite being observed across a range of facilities, the presence of the flow features has not been discussed in the literature. Furthermore, because schlieren visualisation provides only spanwise-integrated information, the exact spanwise location of these features is not known. Since the physical cause for these artefacts has not been identified, it is difficult to assess their impact on the tunnel flow field or on experimental data obtained in these facilities.

For a validation study in Supersonic Wind Tunnel No. 1 at Cambridge University Engineering Department, the Mach 2.5 flow in the empty tunnel is carefully characterised [4]. As part of this process, schlieren images are captured using several different exposure times. Figure 1a, with an exposure time of 0.1 ms, shows the boundary layers on the tunnel floor and ceiling, as well as some weak Mach waves. These waves are generated by imperfections in the floor and ceiling, such as pressure taps or the junctions between the liner blocks which form these surfaces. The weak nature of the waves in this facility has been demonstrated by the small Mach number variation over the test section (deviations of 0.02 from a mean value of 2.48), and the fact that they do not disturb the floor or ceiling boundary layers [4].

When the exposure time is reduced to 1.1 µs, as shown in Fig. 1b, turbulent eddies become visible. These are thought to be inside the sidewall boundary layers. In addition, two subtle streamwise-coherent flow features, indicated by red arrows in the figure, can be resolved. These flow structures lie slightly above and below the tunnel centre-height.

The features captured in Fig. 1b appear similar to the artefacts observed in the literature, which suggests that there may be a common underlying cause. For this reason, an investigation was launched to determine the origin and significance of these flow disturbances. In particular this study aims to answer the following questions: What is the cause of the features? Where across the tunnel span are the features located, and how confined are they in this direction? How strong are the features, and how do they impact the wider flowfield? In which types of facilities might these

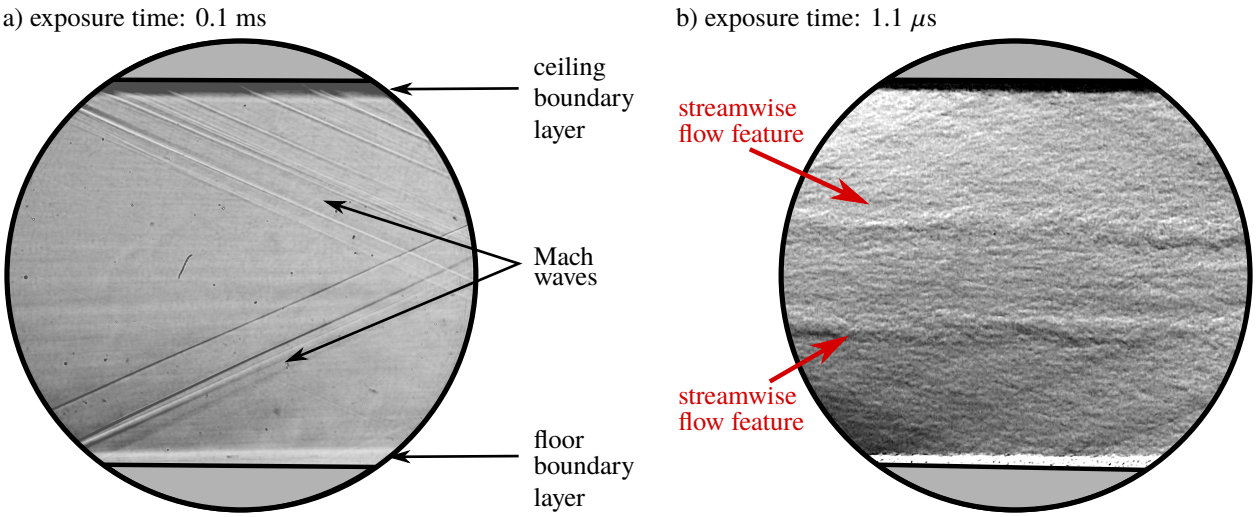

Fig. 1 Schlieren image of the empty wind tunnel with a horizontal knife edge and an exposure time of a) 0.1 ms, and b) 1.1 μs. Flow direction is from left to right.

features be expected to exist? Is it possible to eliminate the features from the flow?

This paper aims to answer these questions by closely studying RANS computations alongside physical experiments of the wind tunnel flow.

II. Research Methodology

A. Wind tunnel experiments

Experiments are performed in Supersonic Wind Tunnel No. 1 at Cambridge University Engineering Department. This is a blow-down wind tunnel, driven by a high-pressure reservoir. The empty wind tunnel configuration used in this study is illustrated in Fig. 2. The nozzle blocks, marked in Fig. 2b, can be interchanged to produce Mach numbers in the range 0.7 to 3.5. For the current study, the tunnel is operated with a symmetric full-nozzle configuration with a nominal freestream Mach number of 2.5. The stagnation pressure is set to 308 ± 1 kPa and the operating stagnation temperature is measured as 285 ± 5 K; this corresponds to a nominal unit Reynolds number of 31×10^6 m^{-1}.

Several experimental techniques are used to probe the flow. A z-type schlieren system with a horizontal knife-edge enables visualisation of spanwise-averaged density gradients associated with flow features in the working section. The schlieren images are captured using a Photron Fastcam Nova S6 camera, which features shutter speeds as fast as 0.2 μs [5]. However, the limited intensity of the point light-source used for this technique sets a minimum exposure time of 1.1 μs in practice.

Surface oil-flow visualisation is also performed to reveal the skin friction line topology and identify any regions of separation. This is an intrusive method and there is a small error due to oil-flow producing an inaccurate indication of separation location, by about 0.2 boundary-layer thicknesses = 0.8 mm [6].

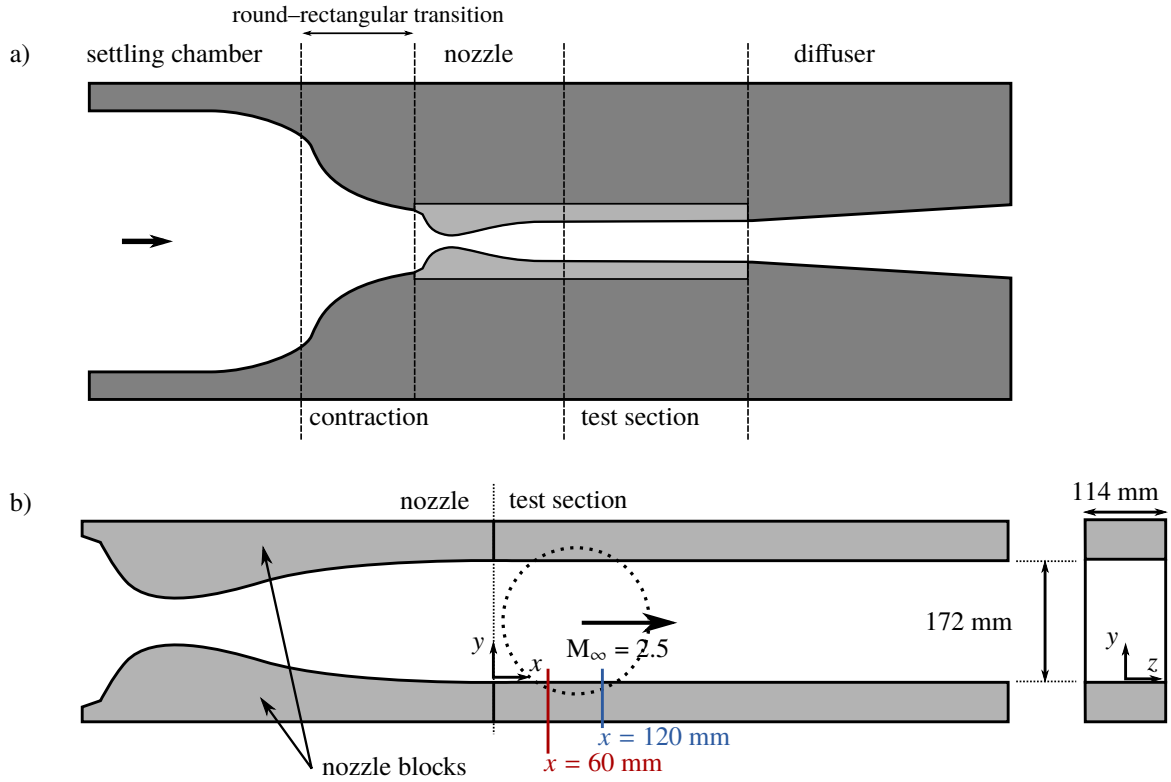

Fig. 2 Tunnel setup: a) overall tunnel infrastructure. b) detail of test section, showing dimensions and coordinate system. The dashed circle corresponds to a window in the tunnel wall providing optical access.

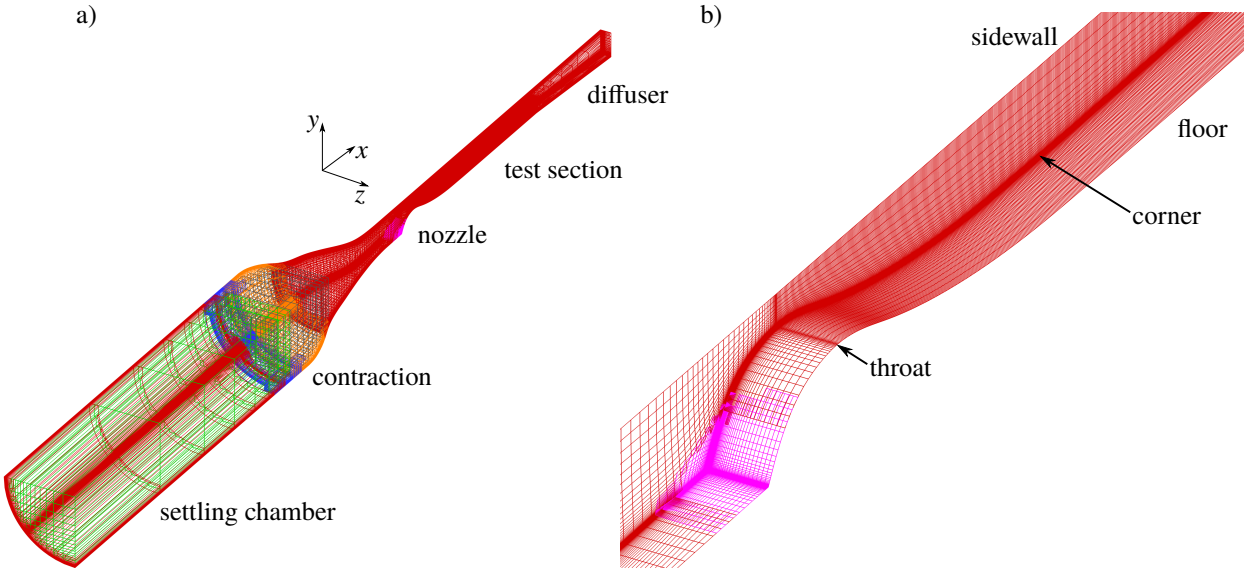

Fig. 3 Representation of mesh used in computations to simulate physical tunnel: a) isometric view of entire mesh; b) surface grid in nozzle and start of test section.

Steady-state surface pressure measurements are performed using static pressure taps with 0.3 mm diameter. The taps are located across the tunnel sidewall, allowing the pressure distributions over this surface to be measured to an accuracy of ±1%.

The streamwise flow velocity, u, is measured by laser Doppler velocimetry (LDV). The flow is seeded with paraffin in the settling chamber. Previous measurements in this facility of particle lag through a normal shock have placed the seeding droplet diameter in the range 200 − 500 nm [7]. The measured velocities have an error of 2%, due to the finite number density of seeding particles and due to the laser optics. In practice, laser Doppler velocimetry is not precisely a point-measurement technique, since velocities are averaged over a nominal ellipsoidal probe volume which spans 0.1 mm in the streamwise and vertical directions, and 2 mm in the spanwise direction. The positional accuracy of this probe volume is, approximately, $\Delta x \approx 0.2$ mm, $\Delta y \approx 0.005$ mm, and $\Delta z \approx 0.1$ mm.

LDV is used to conduct boundary-layer traverses with a spatial resolution of around 0.1 mm. The measured velocity data is then fitted to theoretical profiles. A Sun & Childs (1973) fit [8], adapted to include a van Driest compressibility correction, is used for the outer layer; this combines a log-law of the wall region with a Coles wake function. The viscous sublayer is modelled using a Musker (1979) fit [9]. These fitted profiles are then used to calculate characteristic boundary-layer integral parameters. This avoids errors caused by poor measurement resolution near the wall and therefore provides a more accurate estimate of boundary-layer parameters. These integral boundary-layer properties (displacement thickness, δ_i, momentum thickness, θ_i, and shape factor, H_i) are determined in their incompressible forms, as these are less sensitive to variations in Mach number and require fewer assumptions to calculate from raw velocity data [10]. The LDV data obtained in this study typically has around 40 measurement points within the boundary layer and the closest data point to the wall is at around $y^+ = 80$. This corresponds to an uncertainty in integral parameters of around 5% for an equilibrium turbulent boundary layer [11].

B. RANS computations

The physical experiments are complemented by RANS simulations of the flow in this facility. From the computations, it is possible to extract flowfield data which can not be accessed by experiments alone, and which might be expected to provide useful information about the flow features under investigation. Since the nature of these features is unknown, it is important to model the entire wind tunnel in order to establish their cause.

For this type of study, it is essential that the computations faithfully represent the flow in the physical wind tunnel. This is achieved by calibrating the simulations using comprehensive flow characterisation data, as detailed in reference [4]. Only one quarter of the tunnel is modelled since it is, in theory, top-bottom and left-right symmetric. The Chimera overset grid technique [12] is used to create a smooth mesh in the contraction and at the sharp corner upstream of the nozzle. The final grid system, shown in Fig. 3, is created using the mesh generation software Pointwise [13], contains 181.7M points across seven grids. A viscous wall spacing of 1.5×10^{-7} m is used with a growth rate of 5%; this

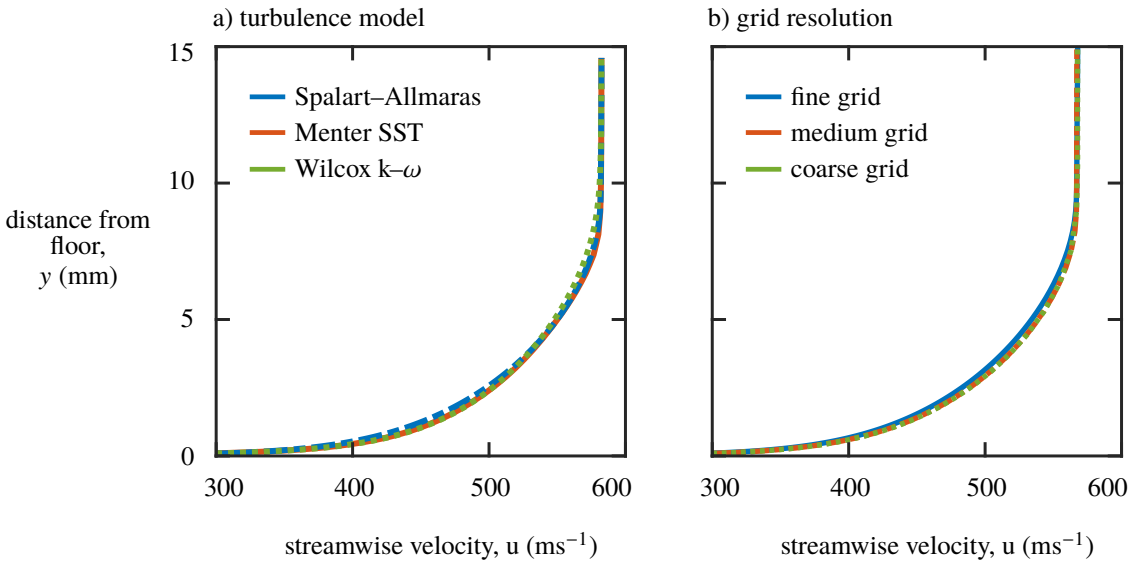

Fig. 4 Floor boundary-layer profiles computed on the centre span at x = 60 mm: a) comparison of profiles for the Spalart–Allmaras, Menter SST and Wilcox k–ω turbulence models; b) comparison of profiles for the coarse, medium and fine grids.

produces $y^+ < 1$ at the first point from the wall.

The solver OVERFLOW 2.2l [14] is used to solve the RANS equations using the third-order accurate upwind finite difference HLLC scheme [15] combined with the Koren limiter [16]. The time integration uses an unfactored SSOR implicit solution algorithm [17].

Centre-span floor boundary-layer profiles using Spalart–Allmaras [18, 19], Menter SST [20, 21], and Wilcox k–ω [22, 23] turbulence models were compared (Fig. 4a). The differences between these profiles are minimal, as expected for an attached boundary layer, which suggests that computations of this relatively simple flow appear to be insensitive to the turbulence model used. Therefore, the Spalart–Allmaras model is chosen due to its robustness and low computational cost. The quadratic constitutive relation (QCR-2013) is used for improved prediction of turbulent stress anisotropies [24, 25].

To conduct a grid resolution study while maintaining the point distribution of the original grid, every other point is removed to create a medium grid (22.9M points), and every other point is removed from the medium grid to produce a coarse grid (2.9M points). Figure 4b shows the centre-span boundary layers on the test section floor for the three grid levels. The three velocity profiles are coincident, indicating that the centre-span profiles have reached grid convergence.

The accuracy of computations is evaluated using a range of characterisation data, in order to test how well the physical wind tunnel flow is captured. In particular, this is assessed by comparing computational data with the experimentally-obtained pressure profile through the test section, the velocities across the channel cross-section, and the profile of the boundary layers growing along the walls. This process is described in detail in Ref. [4], and the key results are summarised below.

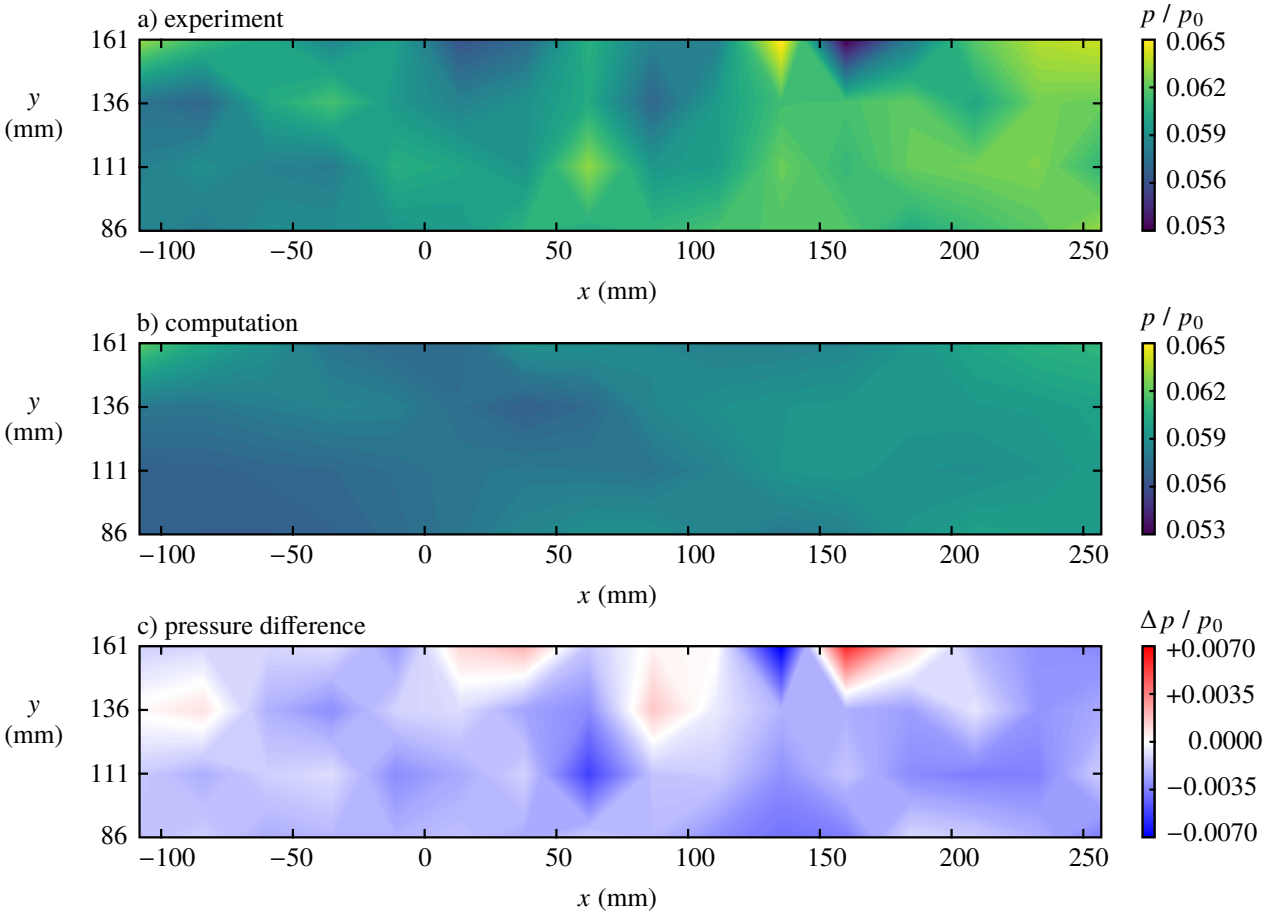

Fig. 5 Static pressure distributions along the wind tunnel sidewall: a) experimental data, b) computational data, and c) calculated difference between experimental and computational pressures. Adapted from [4].

A comparison of the computational and experimental sidewall pressure distributions is presented in Fig. 5. The computations appear to slightly under-predict the pressure, with the flow expanding to a lower pressure and a higher Mach number than the experiment. However, the difference between experimental and computational static pressure ratios, p/p_0, is around 3×10^{-3}, which corresponds to a small Mach number discrepancy of about 1.5%.

The streamwise velocity across the tunnel cross-section was measured using laser Doppler velocimetry (Fig. 6a), and compared to equivalent computational data from Fig. 6b. Unfortunately, high-quality data can not be obtained over the entire cross-section due to insufficient seeding particles in some regions. The resulting gaps in data are marked in Fig. 6a with light grey. On first glance, the computations appear to be consistent with the experimental data – there is a large core region, the floor/ceiling boundary layers are spanwise-uniform with similar thicknesses, and there are significant variations in the thickness of the sidewall boundary layer. A more quantitative measure is obtained by calculating the difference between the two velocity distributions in Fig. 6c. The velocities at most locations differ by no more than 10 ms^{-1}, or 1.7% of the freestream velocity. The notable exception is the sidewall boundary layers, where the

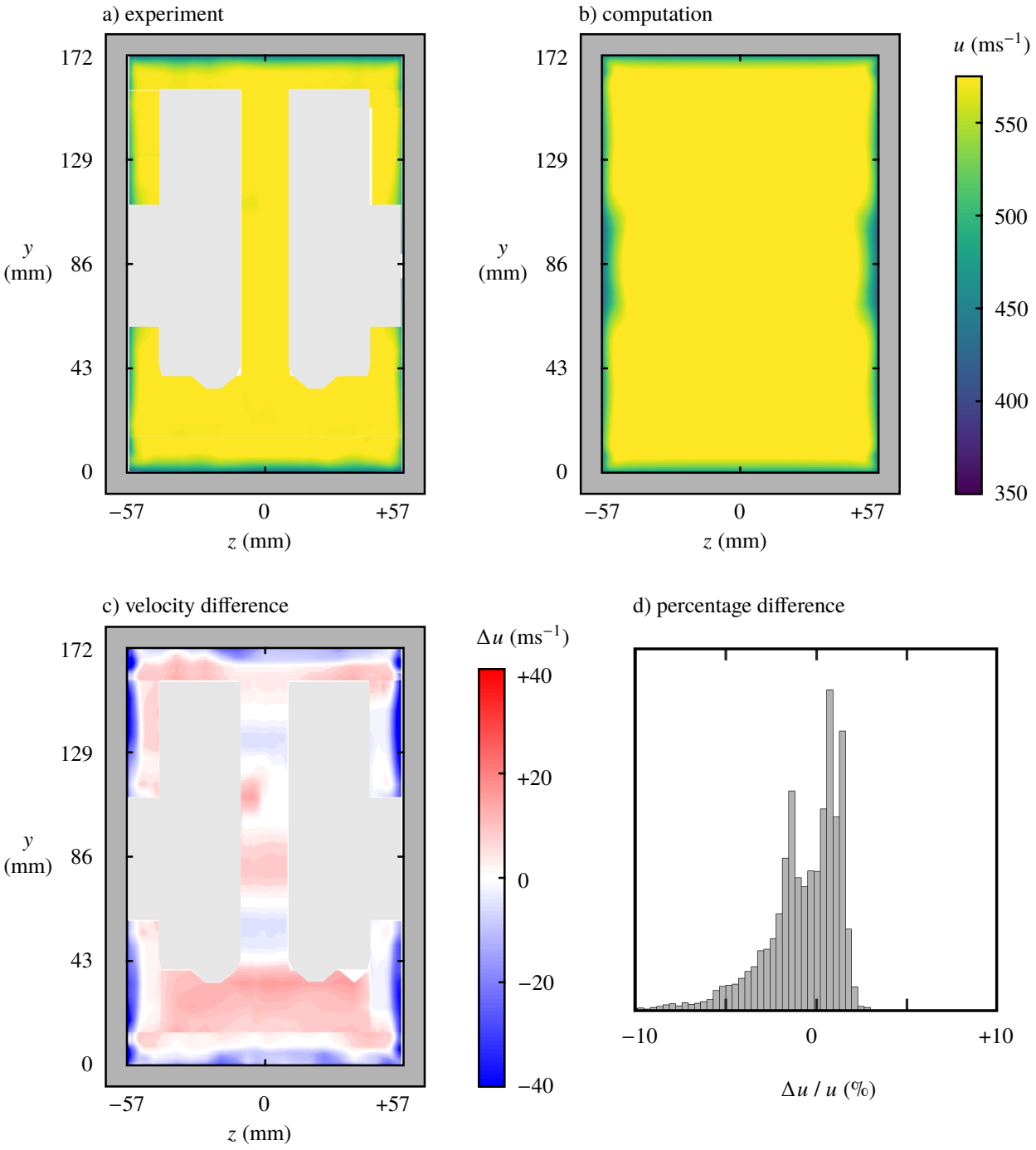

Fig. 6 Comparison between computations and experiment of the streamwise velocity at $x = 120$ mm: a) laser Doppler velocimetry measurements of streamwise velocity; b) streamwise velocity extracted from computations; c) difference between the computed velocity and equivalent experimental data; d) histogram of percentage velocity differences between computations and experiment. Light grey regions correspond to regions where high-quality velocity data could not be obtained. Adapted from [4].

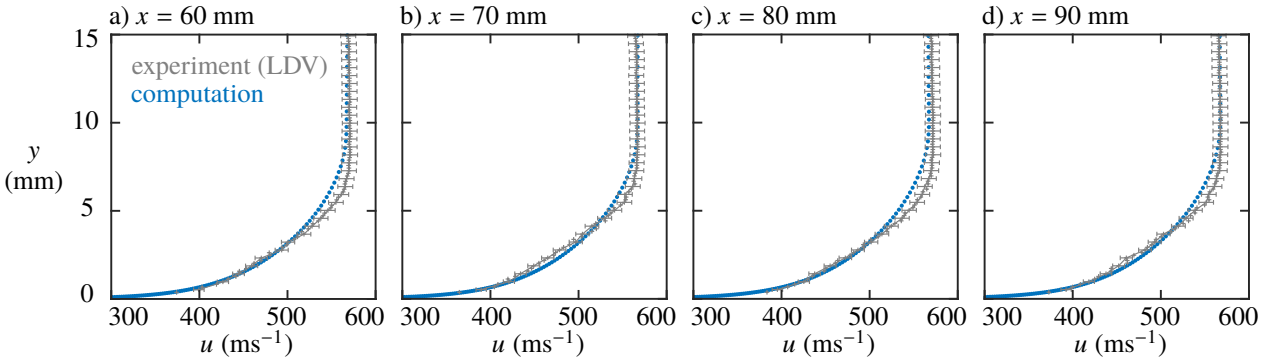

Fig. 7 Comparison between computational and experimental floor boundary-layer profiles, on the tunnel centre span. The profiles are shown for: a) x = 60 mm, b) x = 70 mm, c) x = 80 mm, and d) x = 90 mm. Error bars on every third data point for clarity. Adapted from [4].

Table 1 Incompressible floor boundary-layer parameters, along the tunnel centreline. These correspond to velocity profiles presented in Fig. 7.

	experiment				computation			
x (mm)	δ (mm)	δ_i^* (mm)	θ_i (mm)	H_i	δ (mm)	δ_i^* (mm)	θ_i (mm)	H_i
60	7.49	0.97	0.73	1.34	8.43	0.96	0.74	1.30
70	7.59	1.03	0.76	1.35	8.49	0.96	0.74	1.29
80	7.70	1.05	0.78	1.36	8.63	0.97	0.75	1.29
90	7.71	1.05	0.78	1.35	8.77	0.99	0.77	1.29

discrepancy with experiment can be twice this large. However, Fig. 6d shows that 95% of data points lie within 4% of experimental velocity measurements.

Measurements of the floor boundary-layer profile on the centre span are assumed to be representative of the boundary layers growing along the wind tunnel walls. A comparison between computational and experimental velocity profiles is presented in Fig. 7. The freestream velocity and the general profile shape appear to be in good agreement. However, there is a slight discrepancy towards the edge of the boundary layer, at around $y = 4 - 8$ mm. To quantitatively assess these differences, relevant boundary layer parameters are evaluated for the profiles. The calculated parameters, listed in table 1, show good agreement of displacement thickness (δ_i^*), momentum thickness (θ_i), and shape factor (H_i). The deviations from experimental values are generally on the order of 4%. With a 5% estimated uncertainty in these quantities, the computations do appear to predict these boundary-layer parameters within experimental accuracy.

However, there is a larger discrepancy in the boundary-layer thickness, δ, on the order of 15%. This parameter therefore does not appear to be predicted particularly well by the computations. Whilst the boundary-layer thickness is known to be less robust than the corresponding integral parameters, the differences are believed to be largely due to the discrepancies in velocity near the boundary-layer edge. These discrepancies, which also result in a poor prediction of the shape factor, appear to be systematic, with the computed velocity profile at the boundary-layer edge consistently different to experiment. Nevertheless, whilst the differences are slightly larger than the estimated experimental uncertainties, they

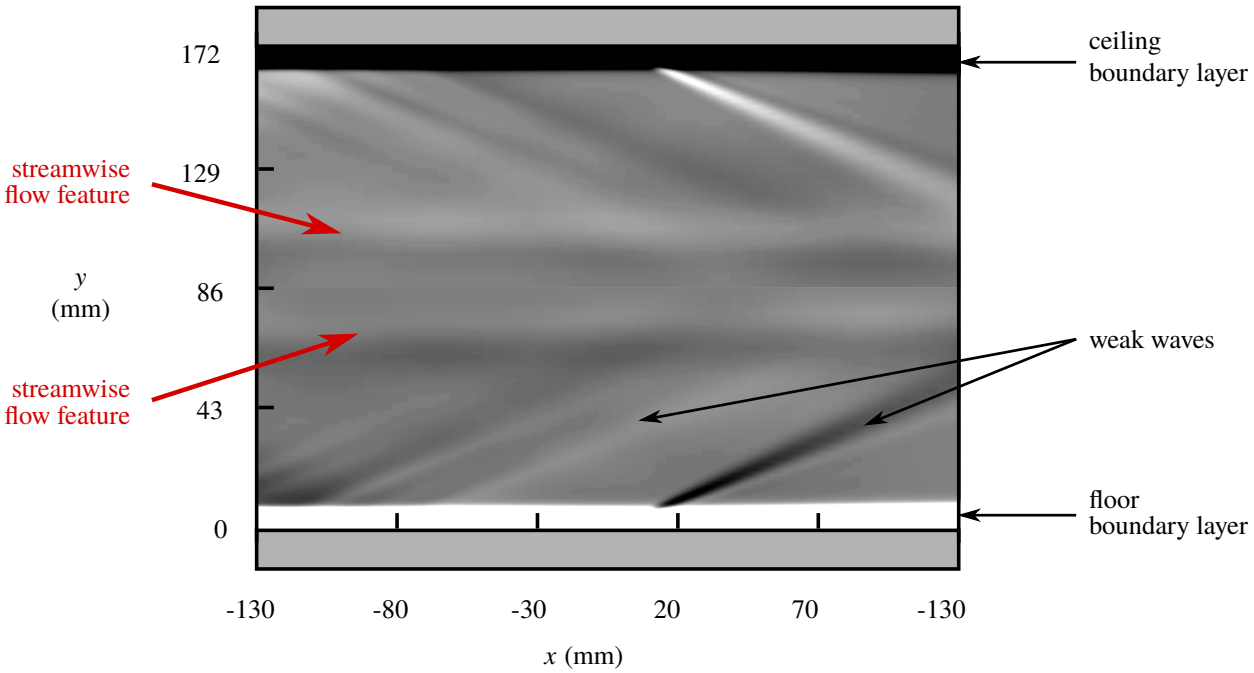

Fig. 8 Numerical, spanwise-averaged schlieren image of the empty wind tunnel extracted from computations. The figure shows density gradients in the y-direction, analogous to a horizontal knife-edge. Flow direction is from left to right.

are relatively minor – the maximum velocity difference is 3% – and perfect agreement is not thought to be vital for the current investigation. Note also that this level of discrepancy is consistent with the typical differences between computed and experimental velocities across the tunnel cross-section, shown in Fig. 6.

Therefore, whilst the precise wind tunnel flow might not be computed exactly, the simulations are thought to capture much of the key flow physics. The comparisons shown in Figs. 5 – 7 indicate that the RANS simulations can be considered, with confidence, to be representative of the physical wind tunnel flow.

A numerical schlieren image of the flow is generated by integrating the vertical density gradient $\partial\rho/\partial y$ across the tunnel span. This visualisation, shown in Fig. 8, captures the floor and ceiling boundary layers along with with weak waves, originating from the tunnel floor and ceiling. These waves are caused by the surface curvature of the floor and ceiling in the nozzle region, with the final, strongest wave due to a discontinuity in curvature at the nozzle exit. Most importantly, however, there appear to be two faint, streamwise-coherent structures that look similar to those observed in the experimental schlieren image (Fig. 1b).

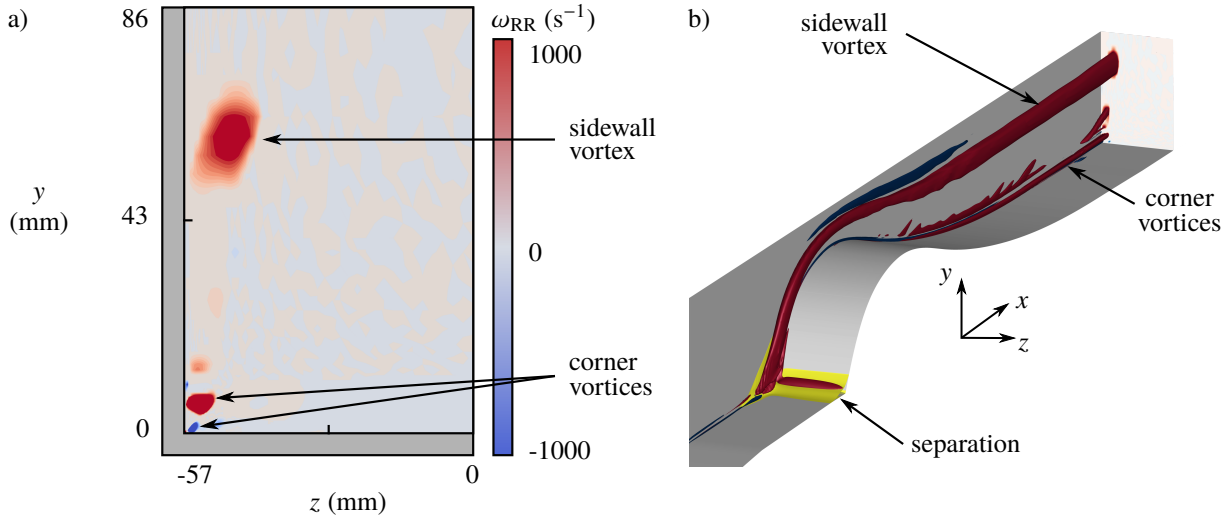

Fig. 9 Rigid-body component of vorticity, ω_{RR}, from RANS computations: a) cross-sectional distribution at x = 120 mm; b) isometric view, showing isosurfaces of ω_{RR} in red and blue, with a region of separation highlighted in yellow. One quarter of the wind tunnel is shown.

III. Results and Discussion

A. Identification of streamwise-coherent features

Figure 9a shows the cross-sectional distribution of streamwise rigid-body vorticity, ω_{RR}, extracted from computations at x = 120 mm. This quantity, defined by Kolář, is calculated by removing the effects of mean shear and of irrotational strain from the vorticity field [26]. It can be seen that there is a region of strong vorticity inside the sidewall boundary layer, 18 mm away from the tunnel centre-height. The vertical location of this 'sidewall vortex' matches the location of the unknown flow features observed in experiment (Fig. 1b) and in computations (Fig. 8). Note that this vortex is separate from the stress-induced counter-rotating vortex pair within the corner boundary layer, labelled as 'corner vortices' in Fig. 9a.

Figure 9a shows that the sidewall vortices appear to originate from a separated flow region immediately upstream of the nozzle block. Here, there is a sharp geometry change at the start of the nozzle, which is shown more clearly in Fig. 10a. The computations predict that the floor boundary layer separates ahead of this sharp corner geometry (Fig. 9b). In order to confirm the physical presence of such a separation, oil-flow visualisation is performed in this region. The resulting skin-friction line topology, shown in Fig. 10b, is indeed consistent with a separated flowfield. The separated region has a streamwise extent of 6 ± 1 mm on the tunnel centre span. This agrees well with the computations, which predict a separation length of 5.2 mm.

The existence of the separation in itself is not entirely surprising. Despite the favourable pressure gradient which exists upstream of the nozzle, the sharp geometry change is topologically similar to a forward-facing step and thus separation of the incoming boundary layer might be expected. However, designers of the wind tunnel facility did not

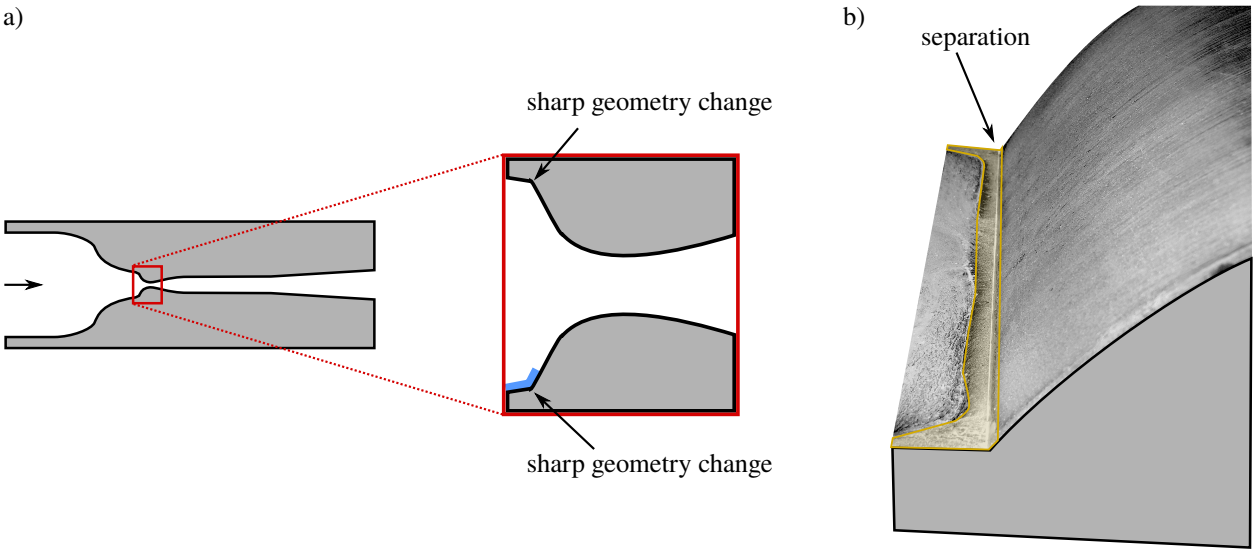

Fig. 10 a) Magnification of Fig. 2b, showing the sharp geometry change upstream of the nozzle. The surface for oil-flow visualisation is marked in blue. b) Surface oil-flow pattern, with the separated region highlighted in yellow.

consider the fact that the separation might have an effect (in this case, a vortex) which persists through the nozzle into the test section.

B. Elimination of sidewall vortices

The RANS computations suggest that the sidewall vortex originates in the separated region upstream of the nozzle. Therefore, removal of this separation should alter, or perhaps eliminate, the vortex. Removing the separation can be achieved by replacing the sharp geometry with a more gentle contour. In order to investigate this hypothesis further, the geometry upstream of the nozzle is redesigned by introducing a fillet. Two different fillet radii are investigated: a 'small' fillet radius of 20 mm and a 'large' fillet radius of 100 mm. According to the numerical simulations, these radii correspond to 5 and 25 local boundary-layer thicknesses, respectively.

The streamwise flow features in Fig. 1b are quite weak, which suggests that a well set-up, sensitive schlieren system is required to capture them. If fillets are introduced to both the floor and ceiling geometries simultaneously, any observed differences in the flowfield could not be definitively attributed to the installed geometry as opposed to an inadvertent change in the sensitivity of the schlieren system. Therefore, the filleted geometry is instead installed along the tunnel floor whilst the original sharp-cornered (or unfilleted) setup is left along the ceiling, as shown in Figs. 11a and 14a. With such a setup, a comparison between the top and bottom halves of the schlieren images directly tests the effects of the installed fillet geometry against the original baseline case.

Small fillet geometry

The small fillet geometry is investigated first. Surface oil-flow visualisation (Figs. 11b and 11c) shows that this setup

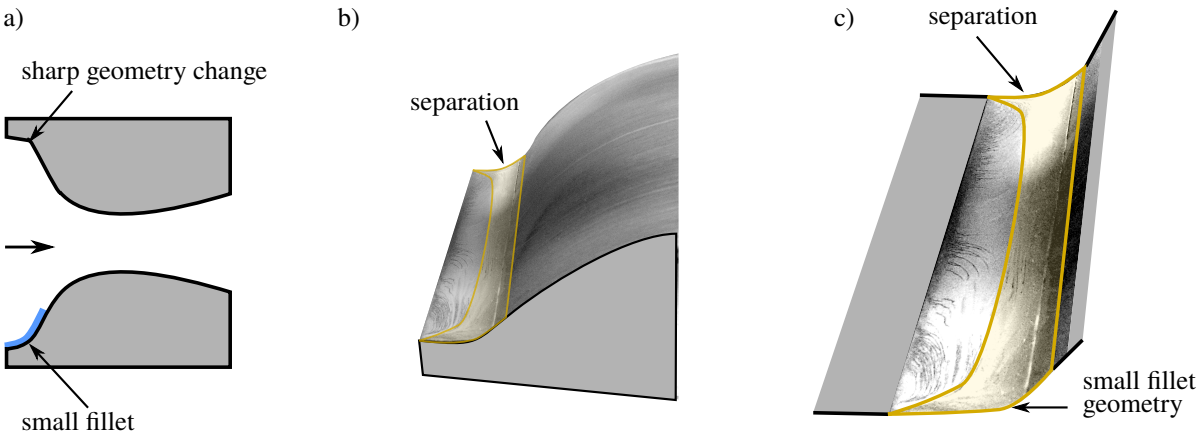

Fig. 11 Experimental tests on the small fillet geometry on the tunnel floor, showing: a) the installed geometry, b) oil-flow visualisation (separated region highlighted in yellow) on the surface marked blue in a, and c) magnified view of separated region from b.

still exhibits separation upstream of the nozzle, albeit with a smaller streamwise extent (5 ± 1 mm). The equivalent computation for the small fillet geometry, shown in Fig. 12a, also predicts separation of the incoming flow. In addition, the computations show that the sidewall vortices remain in the test section and are more or less unchanged, as evident in Fig. 12a. The sidewall vortex marked in Fig. 12b has a rigid-body vorticity distribution almost identical to that determined for the unfilleted geometry (Fig. 9a).

Figure 13a is a numerical schlieren image based on the computations for this setup. The streamwise-coherent density gradients associated with the sidewall vortices are, unsurprisingly, still visible. Schlieren visualisation of the physical wind tunnel flow is presented in Fig. 13b. Weak waves generated by the tunnel's floor and ceiling at the junctions between liner blocks can be discerned. More importantly, the image shows the presence of streamwise-coherent structures of similar strength in both the top and bottom halves of the flow. Both experiments and computations therefore indicate that the small fillet geometry does not remove the separation ahead of the nozzle, and that the sidewall vortices continue to exist in the test section. These findings are consistent with the hypothesised relationship between the sidewall vortices and the separation immediately upstream of the nozzle.

Large fillet geometry

In order to fit the large fillet, geometric constraints require the nozzle to be shifted downstream by 150 mm. The revised setup (Fig. 14a) consists of an unfilleted geometry on the tunnel ceiling and the large fillet on the floor. Here, the oil-flow visualisation on the floor (Fig. 14b) suggests that the smooth contour has been successful at removing flow separation. The computations in Fig. 15a also show that the flow remains attached.

In addition, the CFD results indicate that there is no longer a sidewall vortex for this configuration, as seen in Fig. 15b. The small residual positive vorticity at around y = 43 mm is due to the bulk upwards velocity within the sidewall boundary layer, caused by vertical pressure gradients in the nozzle region [27]. The absence of sidewall vortices

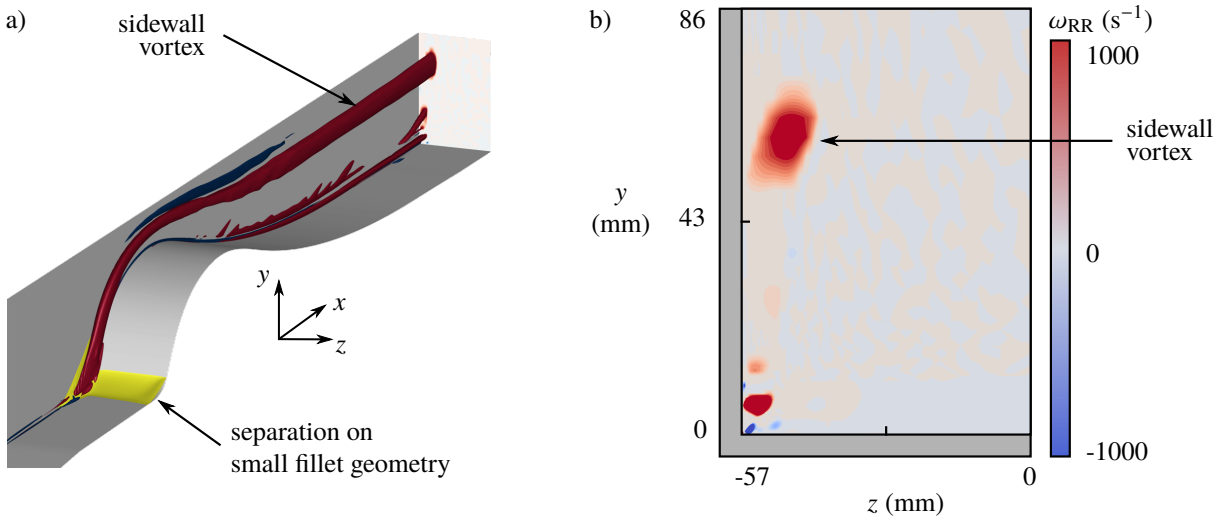

Fig. 12 **Rigid-body component of vorticity, ω_{RR}, from computations of the small fillet geometry: a) isometric view, showing isosurfaces of ω_{RR} in red and blue, with a region of separation highlighted in yellow; b) cross-sectional distribution at x = 120 mm. One quarter of the wind tunnel is shown.**

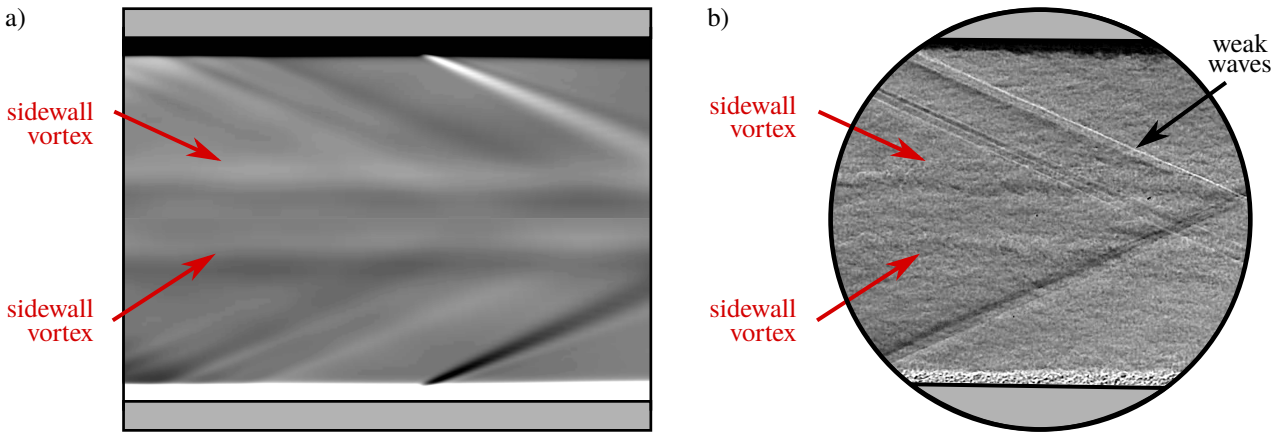

Fig. 13 **Schlieren visualisation of the flow with the small fillet geometry: a) numerical schlieren from computations (floor and ceiling: small fillet); b) experimental schlieren image with 1.1 μs exposure time (floor: small fillet, ceiling: unfilleted). Flow is from left to right.**

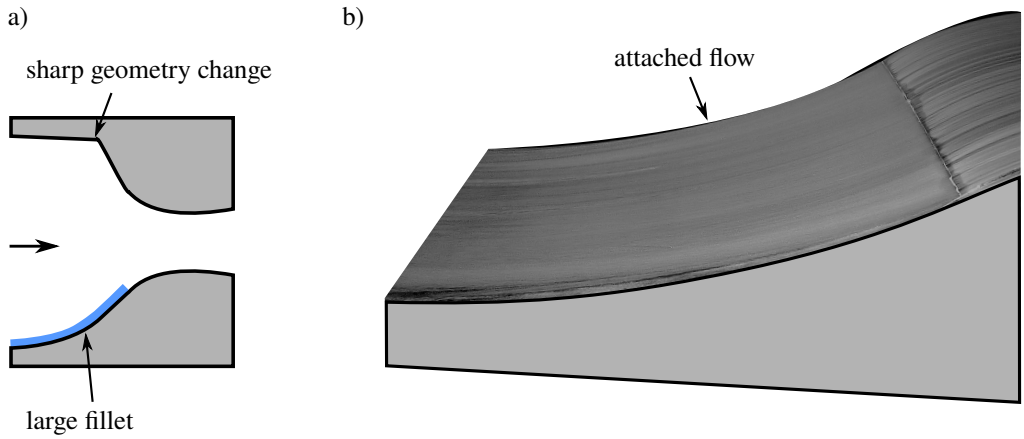

Fig. 14 Experimental tests on the large fillet geometry on the tunnel floor, showing: a) the installed geometry, b) oil-flow visualisation on the surface marked blue in a.

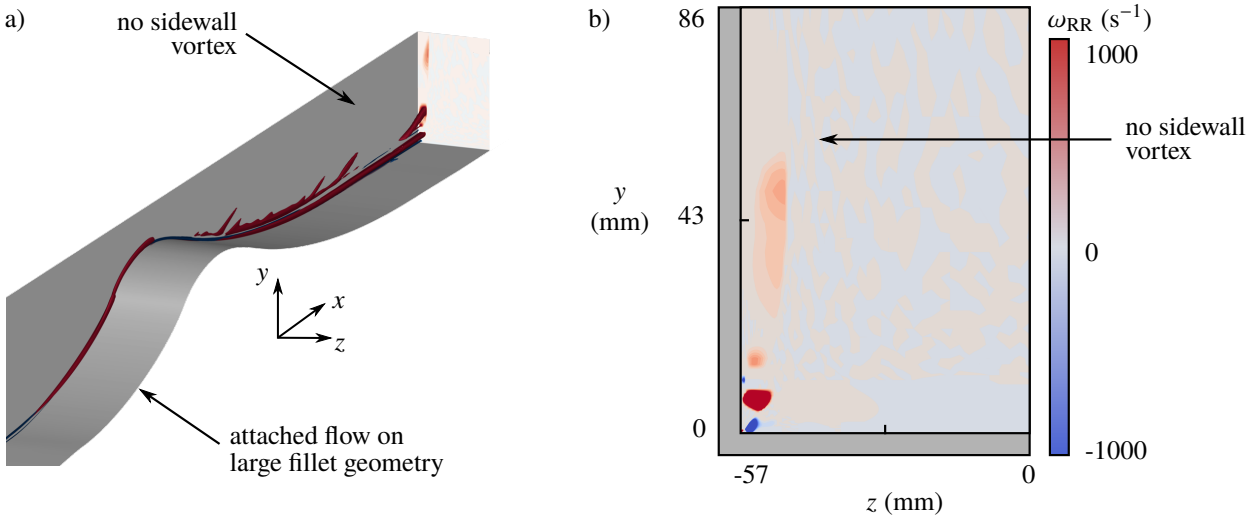

Fig. 15 Rigid-body component of vorticity, ω_{RR}, from computations of the large fillet geometry: a) isometric view, showing isosurfaces of ω_{RR} in red and blue; b) cross-sectional distribution at x = 120 mm. One quarter of the wind tunnel is shown.

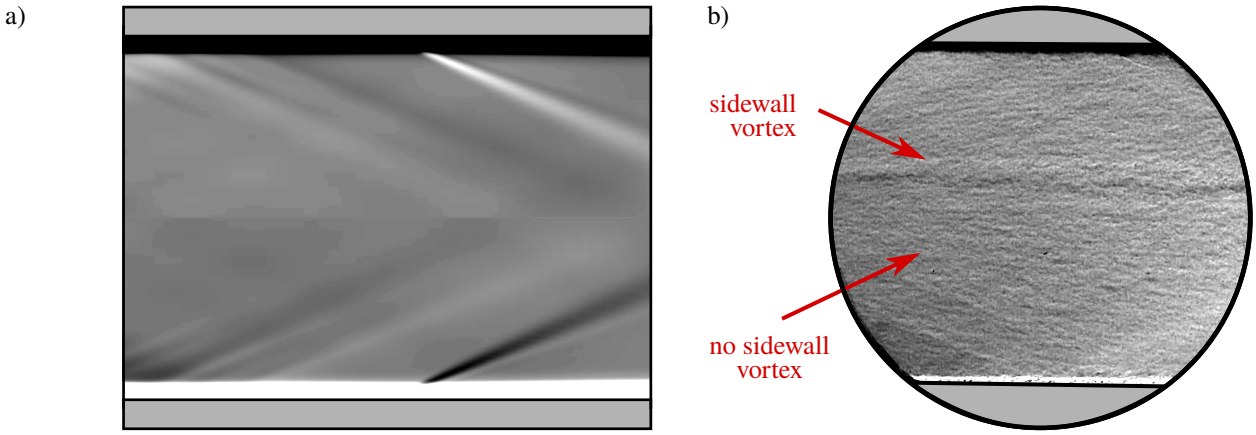

Fig. 16 Schlieren visualisation of the flow with the large fillet geometry: a) numerical schlieren from computations (floor and ceiling: large fillet); b) experimental schlieren image with 1.1 μs exposure time (floor: large fillet, ceiling: unfilleted). Flow is from left to right.

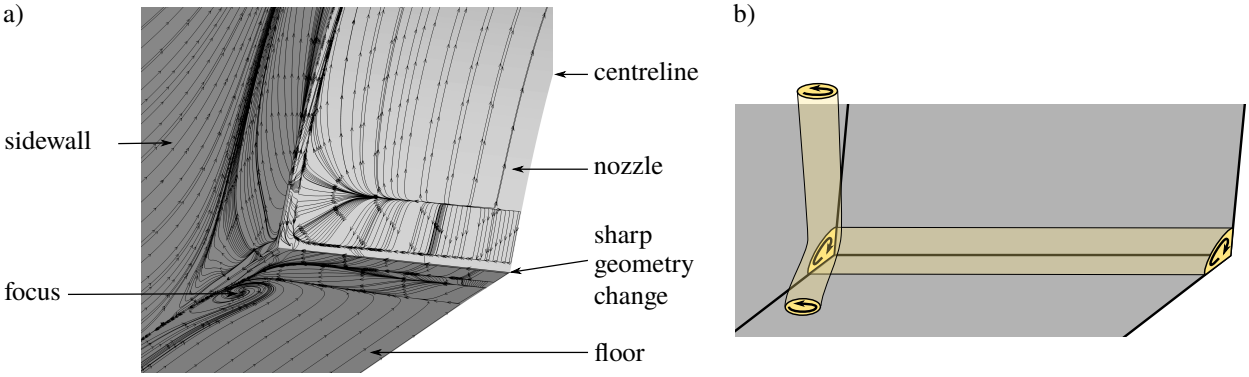

Fig. 17 Vortex topology associated with separation ahead of the nozzle: a) skin-friction line topology extracted from RANS computations; b) schematic of corresponding vortex topology.

with the large fillet geometry is supported by the numerical schlieren image in Fig. 16a, where the streamwise-coherent features visible in Figs. 8 and 13a have disappeared.

The experimental schlieren image in Fig. 16b shows a single streamwise-coherent feature in the upper half of the flowfield, which corresponds to sidewall vortices from the separation on the unfilleted tunnel ceiling (Fig. 14a). However, the lower half of the flowfield does not exhibit any streamwise structures. Both computations and experiment therefore conclude that the elimination of the separation ahead of the nozzle coincides with the disappearance of the streamwise-coherent structures in the test section, providing further evidence of the close causal link between these flow features.

C. Origin of sidewall vortices

The experiments and computations both provide strong evidence that the sidewall vortices are intimately coupled to the separated region ahead of the nozzle. It is difficult to ascertain the precise production mechanism without higher-fidelity

simulations or optical access to the upstream half of the test section. However, the well-established relationship between three-dimensional separation and vortex production provides some clues to the origin of the studied feature.

On the tunnel centre-span, the recirculating region of the separation bubble can be treated as a spanwise-aligned vortex. In physical three-dimensional flows, it is extremely rare (or perhaps even impossible) for this vortex to start and end on the sidewalls to form a closed separation [28]. Instead, the local skin-friction line topology from computations, shown in Fig. 17a, reveals a more complex picture. There is a focus present on the floor, slightly upstream of the separation line as it approaches the sidewall. This focus is the footprint of a tornado-like vortex which is then advected by the flow. The corresponding schematic representation, shown in Fig. 17b, presents this vortex topology, which is well-established in the literature [28]. It is important to note, however, that the ability to accurately predict such vortex topologies using steady RANS simulations with a relatively simple turbulence model has not been verified. Moreover, foci cannot be resolved in the experimentally-observed oil-flow patterns on the floor (Figs. 10b and 11c). This suggests that confirmation of the exact flow topology requires a critical-point analysis of high-quality surface oil-flow information from the floor and sidewalls, which is experimentally challenging and outside the scope of this study.

Whatever the precise flow topology, a streamwise-aligned vortex is produced by the separated region. This vorticity is advected by the flow through the two-dimensional nozzle, and is intensified by a vortex-stretching mechanism due to the large streamwise velocity gradient [29]. Figure 9 shows that, as the vortex passes through the nozzle, it also moves away from the floor towards the tunnel centre-height. This trajectory is consistent with known secondary flows within the sidewall boundary layers, which are directed from the corners towards the centre-height [27].

D. Impact of sidewall vortices

The influence of sidewall vortices on the overall flow can be assessed by comparing the streamwise velocity distribution between cases with and without the vortices. Unfortunately, the locations of the vortices correspond to the gaps in velocity data from Fig. 6a where high-quality measurements can not be obtained. As a result, experiments can not be used for this analysis. Instead, the likely impact of the sidewall vortices is studied using the RANS simulations.

The computed streamwise velocity distributions in the two cases which do exhibit sidewall vortices (Fig. 18a for the unfilleted geometry and Fig. 18b for the small fillet) appear to be very similar to each other. These flows both exhibit a bulge in the sidewall boundary layer close to the tunnel centre-height, at the location of the sidewall vortices.

Figure 18c displays the flow for the large fillet geometry, where there are no sidewall vortices. The core flow, floor boundary layer and corner regions have not changed significantly from Figs. 18a and 18b. However, the sidewall boundary layer does look slightly different. This difference is highlighted by comparing velocity profiles at $y = 70$ mm in Fig. 19, and the associated integral boundary-layer properties (table 2). These parameters show that the shape factor is about 1.4 for all three geometries, but there is a significant variation in the boundary-layer thickness. In fact, the sidewall boundary layer is 37% thicker when the sidewall vortices are present (the unfilleted and small fillet setups), as

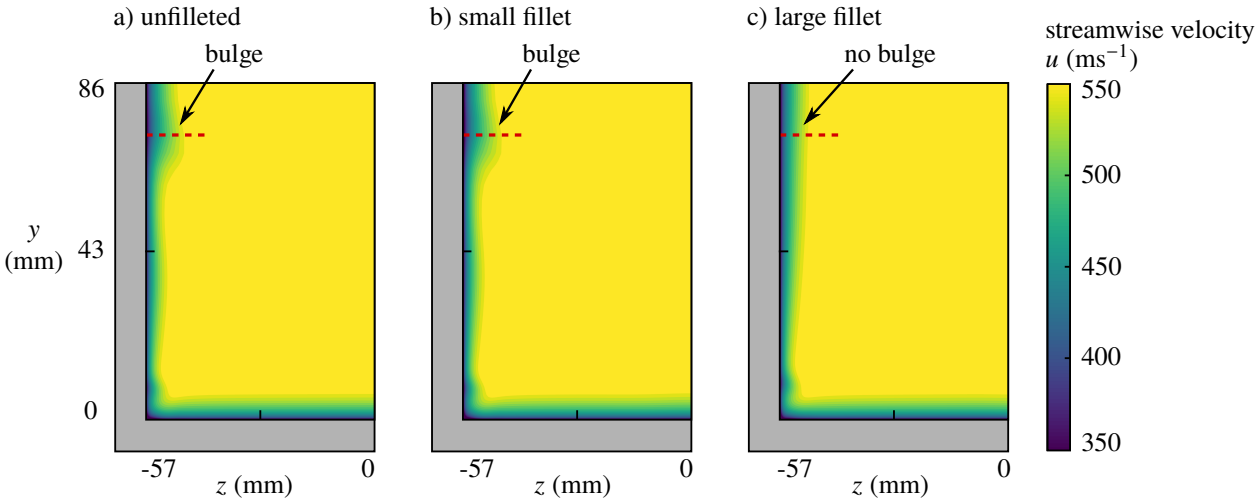

Fig. 18 Streamwise velocity at $x = 120$ mm, from RANS simulation of wind tunnel for a) the unfilleted geometry, b) the small fillet geometry, and c) the large fillet geometry. One quarter of the wind tunnel cross-section is shown. The dashed line indicates the location of boundary-layer profiles in Fig. 19.

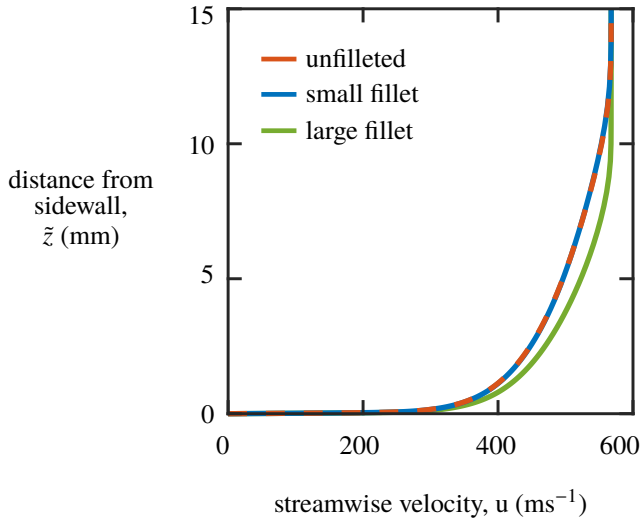

Fig. 19 Sidewall boundary-layer profile, at $y = 70$ mm and $x = 120$ mm, from RANS simulations of the three setups.

Table 2 Boundary-layer parameters for sidewall boundary-layer profiles, at y = 70 mm and x = 120 mm. These correspond to the velocity data presented in Fig. 19.

	δ (mm)	δ_i^* (mm)	θ_i (mm)	H_i
unfilleted geometry	9.27	1.54	1.09	1.41
small fillet geometry	9.28	1.53	1.09	1.41
large fillet geometry	6.70	1.11	0.78	1.42

compared to when the large-radius fillet is used. These differences in sidewall boundary-layer profile highlight the impact of the sidewall vortices on the flow.

Therefore, the sidewall vortices are not a very strong feature, having only a local effect on the flow. This explains why these flow structures have not been noticed earlier despite the widespread use of interchangeable, two-dimensional nozzle geometries, which generally feature sharp corners. Nevertheless, these vortices are significant since they contribute to flow non-uniformity, and since they might make the local region of the sidewall boundary layer more susceptible to flow separation in adverse pressure gradients. As a result, studies on shock–boundary-layer interactions which focus on the response of the sidewall boundary layer are likely to be affected by the vortices, which will introduce additional three-dimensionality to the flow field.

IV. Conclusions

Streamwise-coherent features have been identified in a Mach 2.5 supersonic flow in a wind tunnel with rectangular cross-section. RANS computations of the physical tunnel flow indicate that these features are vortices inside the sidewall boundary layers. In their vicinity, these vortices can thicken the sidewall boundary layer by as much as 37%. The vortices originate from a separated flow region upstream of the nozzle, which is caused by the local surface geometry changing sharply.

This separation can be modified by replacing the sharp geometry change with a more gentle contour. A fillet radius of 5 local boundary-layer thicknesses is insufficient to prevent separation. However, a larger fillet radius (25 boundary-layer thicknesses) enables the incoming boundary layer to remain attached. Both computations and experiments show that the sidewall vortices are present for the small fillet geometry; however, they no longer exist for the large-radius fillet when the flow stays attached upstream of the nozzle. These findings further support the hypothesised close relationship between the sidewall vortices and the separation ahead of the nozzle.

The separation upstream of the nozzle, and thus the presence of sidewall vortices, are now known to be related to the sharp geometry changes at the upstream end of the two-dimensional nozzle blocks. Many supersonic wind tunnels use either interchangeable nozzle blocks, similar to the Cambridge facility, or adjustable nozzles [30]. Geometric constraints often require a sudden geometry change at the start of the nozzle in these types of facility. Wind tunnels which feature sharp corners are expected to be particularly susceptible to separation of the incoming boundary layer, and

therefore production of sidewall vortices. Indeed, schlieren images which show similar streamwise-coherent features can be found in a number of publications originating from such facilities [1–3].

It has been shown that this type of sidewall vortex can be avoided by replacing sharp geometry changes in the upstream, subsonic section of the wind tunnel nozzle with a more gentle contour. When these modifications are not feasible, experimentalists should consider the possible presence of sidewall vortices when interpreting schlieren images and other data, particularly relevant in the context of the increasing sensitivity of high-speed cameras. Furthermore, when validating numerical codes using experimental data, a knowledge of the nozzle geometry is necessary to predict the sidewall vortices and resultant boundary-layer shape in facilities where these structures do exist.

Funding Sources & Acknowledgements

This material is based upon work supported by the US Air Force Office of Scientific Research under award FA9550–16–1–0430. The authors would like to thank D. Martin, A. Luckett and C. Costello for operating the blow-down wind tunnel. The wind tunnel is part of the UK National Wind Tunnel Facility and their support is gratefully acknowledged.

References

[1] Skews, B., "Aspect ratio effects in wind tunnel studies of shock wave reflection transition," *Shock Waves*, Vol. 7, No. 6, 1997, pp. 373–383. doi:10.1007/s001930050092.

[2] Ristić, S., "Flow visualization techniques in wind tunnels: Optical methods (Part II)," *Scientific Technical Review*, Vol. 57, No. 2, 2007, pp. 38–49.

[3] Lu, F., Ali, S., Braun, E., and Maddalena, L., "A modern compressible flow laboratory experience for undergraduates," *49th AIAA Aerospace Sciences Meeting including the New Horizons Forum and Aerospace Exposition*, 2011-0274. doi:10.2514/6.2011-274.

[4] Sabnis, K., Babinsky, H., Galbraith, D., and Benek, J., "Flow characterisation for a validation study in high-speed aerodynamics," *2019 Fluid Dynamics Conference*, 2019-3073. doi:10.2514/6.2019-3073.

[5] *FASTCAM NOVA S6/S9/S12 Datasheet*, Photron, Tokyo, Japan, 2020.

[6] Squire, L., "The motion of a thin oil sheet under the steady boundary layer on a body," *Journal of Fluid Mechanics*, Vol. 11, No. 2, 1961, pp. 161–179. doi:10.1017/S0022112061000445.

[7] Colliss, S., "Vortical structures on three-dimensional shock control bumps," Ph.D. thesis, University of Cambridge, 2014.

[8] Sun, C., and Childs, M., "A modified wall wake velocity profile for turbulent compressible boundary layers," *Journal of Aircraft*, Vol. 10, No. 6, 1973, pp. 381–383. doi:10.2514/3.44376.

[9] Musker, A., "Explicit expression for the smooth wall velocity distribution in a turbulent boundary layer," *AIAA Journal*, Vol. 17, No. 6, 1979, pp. 655–657. doi:10.2514/3.61193.

[10] Délery, J., Marvin, J., and Reshotko, E., "Shock-wave boundary layer interactions," Tech. rep., Advisory Group for Aersopace Research and Development (France), 1986.

[11] Titchener, N., Colliss, S., and Babinsky, H., "On the calculation of boundary-layer parameters from discrete data," *Experiments in Fluids*, Vol. 56, No. 8, 2015, p. 159. doi:10.1007/s00348-015-2024-5.

[12] Benek, J., Steger, J., and Dougherty, F., "A flexible grid embedding technique with application to the Euler equations," *6th Computational Fluid Dynamics Conference Danvers*, 1983-1944. doi:10.2514/6.1983-1944.

[13] *Pointwise Version 18.0R4*, Pointwise Incorporated, Fort Worth, TX, 2017.

[14] Buning, P., Jespersen, D., Pulliam, T., Chan, W., Slotnick, J., Krist, S., and Renze, K., *Overflow User's Manual*, NASA Langley Research Center, Hampton, VA, 2002.

[15] Toro, E., Spruce, M., and Speares, W., "Restoration of the contact surface in the HLL-Riemann solver," *Shock Waves*, Vol. 4, No. 1, 1994, pp. 25–34. doi:10.1007/BF01414629.

[16] Koren, B., "Upwind schemes, multigrid and defect correction for the steady Navier-Stokes equations," *11th International Conference on Numerical Methods in Fluid Dynamics*, Springer, 1989, pp. 344–348. doi:10.1007/3-540-51048-6_52.

[17] Tramel, R., and Nichols, R., "A highly efficient numerical method for overset-mesh moving-body problems," *13th Computational Fluid Dynamics Conference*, 1997-2040. doi:10.2514/6.1997-2040.

[18] Spalart, P., and Allmaras, S., "A one-equation turbulence model for aerodynamic flows," *30th Aerospace Sciences Meeting and Exhibit*, 1992-0439. doi:10.2514/6.1992-439.

[19] Allmaras, S., and Johnson, F., "Modifications and clarifications for the implementation of the Spalart-Allmaras turbulence model," *Seventh International Conference on Computational Fluid Dynamics*, ICCFD7-1902, 2012.

[20] Menter, F., and Rumsey, C., "Assessment of two-equation turbulence models for transonic flows," *Fluid Dynamics Conference*, 1994-2343. doi:10.2514/6.1994-2343.

[21] Menter, F., Kuntz, M., and Langtry, R., "Ten years of industrial experience with the SST turbulence model," *4th International Symposium on Turbulence, Heat and Mass Transfer*, 2003, pp. 625–632.

[22] Wilcox, D., "Reassessment of the scale-determining equation for advanced turbulence models," *AIAA Journal*, Vol. 26, No. 11, 1988, pp. 1299–1310. doi:10.2514/3.10041.

[23] Wilcox, D., *Turbulence Modeling for CFD*, 3rd ed., DCW Industries, Incorporated, 2006.

[24] Spalart, P., "Strategies for turbulence modelling and simulations," *International Journal of Heat and Fluid Flow*, Vol. 21, No. 3, 2000, pp. 252–263. doi:10.1016/B978-008043328-8/50001-1.

[25] Mani, M., Babcock, D., Winkler, C., and Spalart, P., "Predictions of a supersonic turbulent flow in a square duct," *51st AIAA Aerospace Sciences Meeting*, 2013-0860. doi:10.2514/6.2013-860.

[26] Kolář, V., "Vortex identification: New requirements and limitations," *International Journal of Heat and Fluid Flow*, Vol. 28, No. 4, 2007, pp. 638–652. doi:10.1016/j.ijheatfluidflow.2007.03.004.

[27] Sabnis, K., and Babinsky, H., "Nozzle geometry effects on corner boundary layers in supersonic wind tunnels," *AIAA Journal*, 2019, pp. 1–4. doi:10.2514/1.J058310.

[28] Délery, J., *Three-dimensional separated flow topology: Critical points, separation lines and vortical structures*, John Wiley & Sons, 2013, Chap. 6, pp. 131–136. doi:10.1002/9781118578544.

[29] Tennekes, H., and Lumley, J., *A first course in turbulence*, MIT Press, 1972, Chap. 3, pp. 83–84.

[30] Pope, A., and Goin, K., *High-speed wind tunnel testing*, John Wiley & Sons, 1965.